

Supporting Information for:
**“Second-harmonic generation enhancement in
monolayer transition-metal dichalcogenides by
an epsilon-near-zero substrate”**

Pilar G. Vianna, Aline dos S. Almeida, Rodrigo M. Gerosa, Dario A. Bahamon,
Christiano J. S. de Matos*

MackGraphe – Graphene and Nanomaterials Research Institute, Mackenzie
Presbyterian University, São Paulo - 01302-907, Brazil.

* E-mail: cjsdematos@mackenzie.br

1. Second-harmonic generation intensity

To quantify the second-order nonlinear response of a 2D material layer, a monolayer of the material can be considered a nonlinear polarization sheet ($\chi_s^{(2)}$) at the interface between two media, in our case, air and the FTO substrate. The second harmonic generation process will depend not only on the nonlinear polarization, but also on the dielectric properties of the surrounding media, which impact the amplitude of the electric field at the interface, as determined by the electromagnetic boundary conditions. With the pump at normal incidence and considering a frequency-dependent refractive indices, the second-harmonic intensity is given by¹:

$$I_{SHG}(2\omega) = 2\epsilon_0 \text{Re}\{n_2(2\omega)\} c \left| \frac{4i(2\omega) n_1^2(\omega) \vec{\chi}_s^{(2)} \hat{e} \hat{e} E_1^2(\omega)}{c[n_1(\omega) + n_2(\omega)]^2 [n_1(2\omega) + n_2(2\omega)]} \right|^2, \quad (1)$$

where ω is the pump frequency, n_1 is the refractive index of the incidence medium, and n_2 is the substrate refractive index, $\vec{\chi}_s^{(2)}$ is the second-order nonlinear sheet susceptibility tensor, \hat{e} is the unit vector associated to the polarization of the pump field, c is the speed of light in vacuum and ϵ_0 is the vacuum permittivity. Note that the refractive indices are taken to be complex. As the medium of incidence is air, we make $n_1(\omega) = n_1(2\omega) = 1$. In

addition, with $|E_1(\omega)|^2 = \frac{I_1(\omega)}{2\epsilon_0 n_1(\omega) c}$, and redefining n_2 as n to avoid confusion with the nonlinear refractive index, we get:

$$I_{SHG}(2\omega) = \frac{8\text{Re}\{n(2\omega)\} [2\omega]^2 |\vec{\chi}_s^{(2)} \hat{e} \hat{e}|^2 I_1^2(\omega)}{\epsilon_0 c^3 |[1 + n(2\omega)][1 + n(\omega)]|^2}. \quad (2)$$

with $I_1(\omega)$ being the pump intensity at the incidence, and in which $|\vec{\chi}_s^{(2)} \hat{e} \hat{e}|^2$ can be replaced with $|\chi_s^{(2)}|^2$, with $\chi_s^{(2)}$ representing the relevant tensor components.

2. Theoretical model

The dielectric function of FTO was described by the Drude free electron model:

$$\epsilon = \epsilon_\infty - \frac{\omega_{p2}}{\omega_2 + i\gamma\omega} \quad (3)$$

where $\varepsilon_\infty = 2.95$, $\omega_p = 1.89 \times 10^{15} \text{ s}^{-1}$ and $\gamma = 0.9 \times 10^{14} \text{ s}^{-1}$ were obtained by fitting experimental transmission spectra. These fittings are shown in Figures 1(A) and 1(B) for the p polarization at 0° and 45° , respectively, while Figures 2(A) and 2(B) show the fittings for the s polarization at 0° and 45° , respectively.

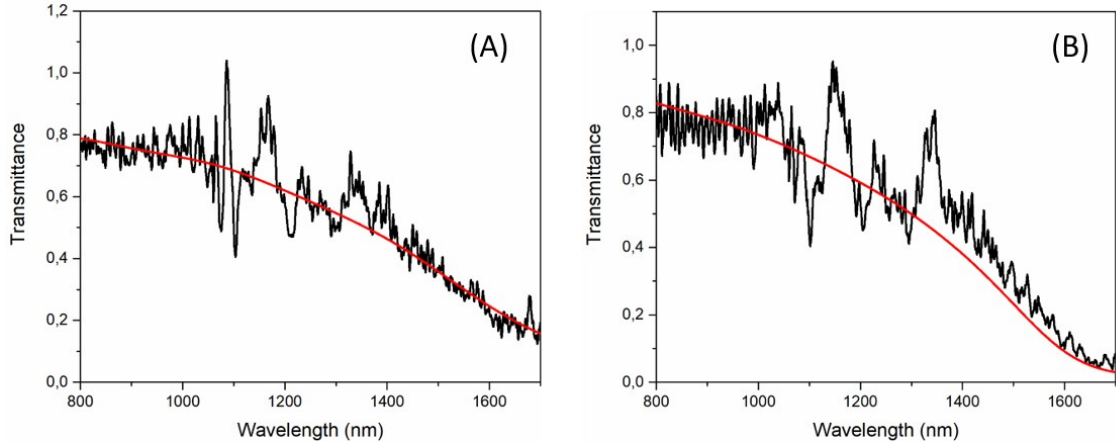


Figure S1: Experimental (black) and theoretical (red) transmittance for the p polarization at 0° (A) and 45° (B).

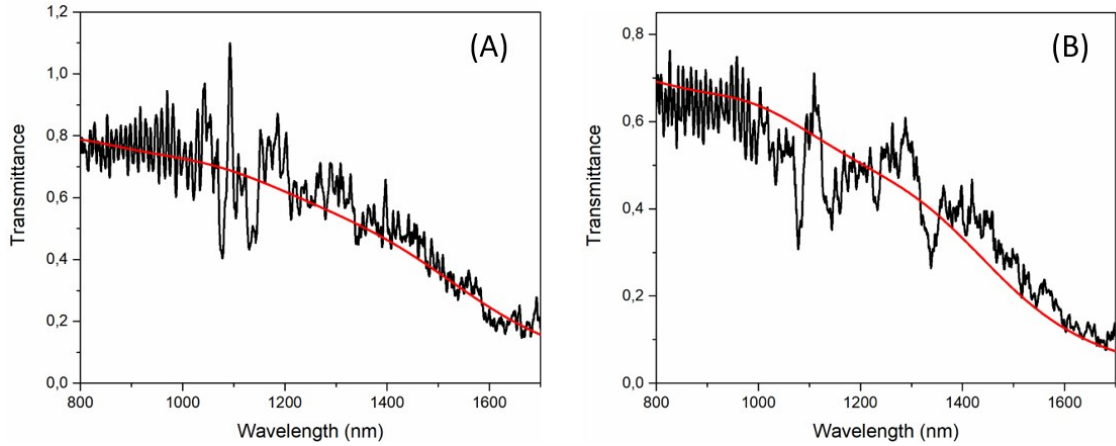


Figure S2: Experimental (black) and theoretical (red) transmittance for the s polarization at 0° (A) and 45° (B).

The sample is modeled as a multilayer system with the z -direction normal to the surface. Layer 1 is a semi-infinite vacuum region ($z > 0$) where the pump source is located. Layer 2 corresponds to the FTO substrate of thickness d ($0 > z > -d$), with a monolayer MoS_2 sheet on top (at $z = 0$) and layer 3 is a semi-infinite glass slide with $z < -d$, where the detector is placed. To evaluate the SHG fields in layer 3, the fundamental fields are first calculated. At normal incidence, the fundamental field at the MoS_2 sheet $\vec{E}^\omega = E^\omega \hat{x} = (1 + r_{13}^\omega) E_i^\omega \hat{x}$ is related to the incident pump field (E_i^ω) by the Fresnel reflection coefficient:

$$r_{13}^{\omega} = r_{12} + \frac{t_{12}t_{21}r_{23}e^{i2k_2d}}{1 - r_{21}r_{23}e^{i2k_2d}}. \quad (4)$$

Note that the coefficients are evaluated at ω , with $r_{12} = \frac{n_1 - n_2 - Z_0\sigma^s}{n_1 + n_2 + Z_0\sigma^s}$ and $t_{12} = \frac{2n_1}{n_1 + n_2 + Z_0\sigma^s}$, which accounts for the monolayer MoS₂ contribution through the

sheet response² $Z_0\sigma^s = \left(\frac{1}{\epsilon_0 c}\right)[-i(\epsilon - 1)\epsilon_0\omega d]$, where $d = 0.65 \text{ \AA}$, is the effective thickness of the monolayer MoS₂ sheet, $\epsilon = 4.97$ is the dielectric function, ϵ_0 is the vacuum permittivity, and n_1, n_2 and n_3 are the refractive indexes for air, FTO and glass, respectively.

Next, the Green's function formalism³ with the infinitesimal vacuum gap approach^{4,5} is used to obtain the SHG fields radiated by the monolayer MoS₂. Using this approach, an infinitesimal vacuum gap is introduced between the MoS₂ layer (at $z = 0^+$) and the FTO layer ($0^- > z > -d$). The suspended MoS₂ sheet generates a downward (-) and an upward (+) SHG field³, defined as:

$$\vec{E}_{\pm}^{\Omega} = i\frac{K_0}{2\epsilon_0}(P_x^{\Omega}\hat{x} \mp P_y^{\Omega}\hat{y})e^{\pm iK_0|z|}, \quad (5)$$

where $K_0 = \frac{\Omega}{c} = \frac{2\omega}{c} = 2k_0$, $P_x^{\Omega} = \epsilon_0 \chi_s^{(2)} \cos(3\theta) \left((1 + r_{13}^{\omega}) E_i^{\omega} \right)^2$ and $P_y^{\Omega} = \epsilon_0 \chi_s^{(2)} \sin(3\theta) \left((1 + r_{13}^{\omega}) E_i^{\omega} \right)^2$. Here, θ is the angle between the crystallographic x' direction (armchair) and the laboratory x coordinate; $\chi_s^{(2)} = \chi_{s'y'y'}^{(2)} = -\chi_{s'yx}^{(2)} = -\chi_{s'xy}^{(2)} = -\chi_{s'yx}^{(2)}$ is the second order sheet susceptibility. In this case, we have assumed a time dependence $e^{-i\Omega t}$ and defined the $\hat{s} = \hat{x}$ and $\hat{p}_{\pm} = \hat{s} \times (\pm \hat{K}_0) = \mp \hat{y}$ polarization. Both polarizations have been treated separately, $u = s, p$, and represent the field in the "m_{th}" layer by a two-element column vector $e_{m,u}$, where the top (bottom) element described the upward (downward) propagation directions. Therefore, the fields above and below MoS₂ can be written³ as $e_{1u}(0^+) = v_u + e_{1u}(0^-) = v_u + M_{13}^u e_{3u}(-d)$. Here, v_u is an SHG field discontinuity introduced by the monolayer, and M_{13}^u is the transfer matrix. Given that there is no

downward (upward) propagation of the SHG field for $z > 0^+$ ($z > d$), for the s polarization we have:

$$\begin{bmatrix} E_{1x}^{\Omega}(0^+) \\ 0 \end{bmatrix} = i \frac{K_0}{2\epsilon_0} P_x^{\Omega} \begin{bmatrix} 1 \\ -1 \end{bmatrix} + M_{13}^x \begin{bmatrix} 0 \\ E_{3x}^{\Omega}(-d) \end{bmatrix} \quad (6)$$

With the transfer matrix defined as:

$$M_{13}^x = \frac{1}{T_{13}} \begin{bmatrix} T_{13}T_{31} - R_{13}R_{31} & R_{13} \\ -R_{31} & 1 \end{bmatrix} \quad (7)$$

It is important to highlight that:

- i. The transfer matrix M_{13}^u is defined between layer 1 at $z = 0^-$ and layer 3, so that the transmission (T_{ij}) and reflection (R_{ij}) terms do not include the MoS₂ sheet response;
- ii. The elements of the transfer matrix are evaluated at $\Omega = 2\omega$. Using Equation 6 for the s polarization and a similar equation for the p polarization, the field in layer 3, is obtained:

$$\vec{E}_3^{\Omega} = i \frac{K_0}{2\epsilon_0} (T_{13}P_x^{\Omega}\hat{x} + T_{13}P_y^{\Omega}\hat{y}) e^{-iK_0|z|} \quad (8)$$

2.1 Monolayer MoS₂ on glass

To compare the SHG fields of the MoS₂/FTO and MoS₂/glass configurations, the SHG fields for MoS₂ on glass were also calculated. The MoS₂/glass sample model has two layers, in which layer 1' is a semi-infinite vacuum layer ($z > 0$) and layer 2' ($z < 0$) is the glass substrate with the monolayer MoS₂ on top. Following the previously detailed methods, we obtain the SHG field in the glass region:

$$\vec{E}_{2'}^{\Omega} = i \frac{K_0}{2\epsilon_0} (T_{1'2'}P_x^{\Omega}\hat{x} + T_{1'2'}P_y^{\Omega}\hat{y}) e^{-iK_0|z|} \quad (9)$$

Where, $T_{1'2'} = \frac{2n_{1'}}{n_{1'} + n_{2'}}$ with $n_{1'}$ and $n_{2'}$ evaluated at $\Omega = 2\omega$, and $P_x^\Omega = \epsilon_0 \chi_s^{(2)} \sin(3\theta) \left((1 + r_{1'2'}^\omega) E_i^\omega \right)^2$ and $P_y^\Omega = \epsilon_0 \chi_s^{(2)} \sin(3\theta) \left((1 + r_{1'2'}^\omega) E_i^\omega \right)^2$. As previously reported, $r_{1'2'}^\omega$ is evaluated at the fundamental frequency and include the MoS₂ sheet response.

2.2 Normalized intensity and optical absorption

In order to compare the transmitted field intensity using both substrates, the MoS₂/FTO SHG intensity ($I(2\omega)_{FTO}$) was normalized by the MoS₂/glass SHG intensity ($I(2\omega)_{glass}$), which we define as the enhancement factor (EF):

$$EF = \frac{I_{123}}{I_{1'2'}} = \frac{I(2\omega)_{FTO}}{I(2\omega)_{glass}} = \frac{|T_{13}(1 + r_{13}^\omega)|^2}{|T_{1'2'}(1 + r_{1'2'}^\omega)|^2} \quad (10)$$

Given the large wavelength in the FTO substrate around the ENZ condition, the reflection coefficient r_{13}^ω remains nearly constant as a function of the dielectric thickness of the FTO substrate. Consequently, the EF dependence on the substrate thickness is given by the transmission function T_{13} . Our results remain valid for a broad range of thicknesses as can be observed in Figure 1B (Main text).

It is also important to mention that, as the complex dielectric function of the substrate is used in our model for Fresnel coefficient calculations, absorption is fully accounted for. Figure S3 presents the calculated transmission $|t_{13}^\omega|^2$, reflection $|r_{13}^\omega|^2$ and absorption $A = 1 - |r_{13}^\omega|^2 - |t_{13}^\omega|^2$ for the fundamental frequency as function of the thickness. Additionally, the classical skin depth $\delta = c/\omega\kappa(\omega)$ for FTO is superimposed as the black curve in each panel.

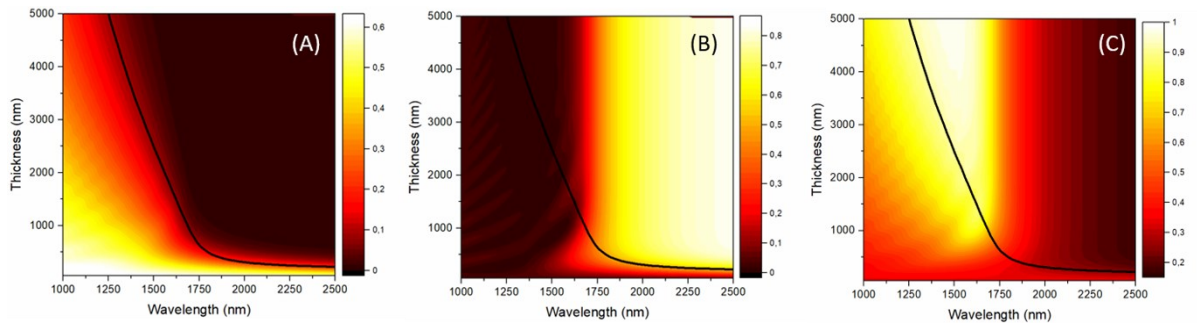


Figure S3. (A) Transmission coefficient $|t_{13}^\omega|^2$. (B) Reflection coefficient $|r_{13}^\omega|^2$. (C) Absorption $A = 1 - |r_{13}^\omega|^2 - |t_{13}^\omega|^2$. The classical skin depth is represented as the black curve in each panel.

From Figure S3, it is possible to observe that the optical absorption around the ENZ point becomes significant for substrates thicker than 1000 nm. Comparing the optical absorption of the ENZ substrate with the EF map (Figure 1B – Main text), it is evident that an increase in the absorption, reduces the EF. In fact, balance between reflection and moderate absorption around the ENZ point is what defines the observed region with high EF values. For the largest enhancement factor of 9.3 at 1680 nm and a thickness of 520 nm, as in our substrate, we have $|r_{13}^\omega|^2 = 0.32$, $A = 1 - |r_{13}^\omega|^2 - |t_{13}^\omega|^2 = 0.47$ and $\delta = 1046.5$ nm; which is evidence that, despite the substrate absorption around the ENZ point, its thickness is smaller than the classical skin depth and the field is not completely attenuated.

3. FTO substrate characterization and processing

FTO (Fluorine doped tin oxide) deposited on SLG (soda lime glass) commercial samples were kindly provided by MSE Supplies LLC. The original FTO thickness was approximately 600 nm with a sheet resistivity of 7-8 Ω/\square . From AFM topography measurements, Figure S3(A), the films were found to have a root mean square (RMS) roughness of 17.8 nm, which virtually prevented the transfer of monolayer transition metal dichalcogenide (TMD) flakes. Therefore, the FTO substrates were polished with fine-grain diamond sandpaper (1 μm grit for 3 min, 0.5 μm grit for 5 min and 0.1 μm grit for 5 min). The AFM topography after polishing can be observed in Figure S3(B), corresponding to an RMS roughness of approximately 1.7nm and a measured thickness of 520 nm.

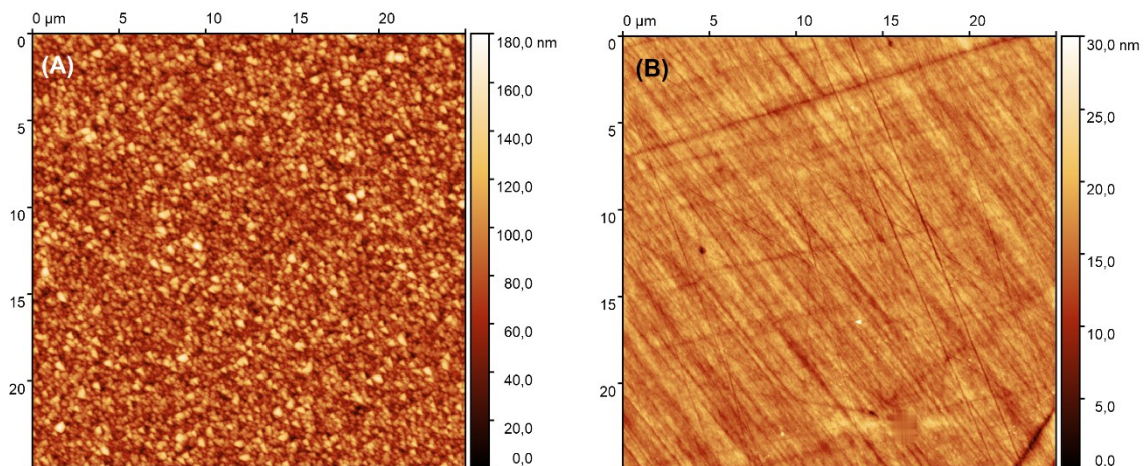


Figure S4: AFM topography images for the original FTO substrate (A) and for the polished FTO substrate (B).

4. MoS₂ and WS₂ Raman and optical microscopy characterization

Raman spectroscopy characterization was performed to confirm the flake thicknesses. Optical microscopy images of the MoS₂ (A) and WS₂ (C) flakes on glass can be observed in Figure S4 and MoS₂ (A) and WS₂ (C) on FTO can be seen in Figure S5.

Figure S4(B) compares spectra from the monolayer and bulk MoS₂ regions of the flake in Figure S4(A), with a wavenumber difference between the A_{1g} to E_{2g}¹ modes of approximately 18.6 cm⁻¹ and 24.5 cm⁻¹, respectively, which is compatible with the literature for monolayer and bulk MoS₂ flakes⁶. The same features were observed for MoS₂ deposited on FTO, as shown in Figure S5(B).

For the WS₂ flakes, the Raman signature can be observed in Figures S4(D) for the material deposited on the glass substrate and in Figure S5(D) for the 2D material deposited on FTO. It is possible to observe characteristic monolayer feature $I_{[2LA(M) + E_{2g}^1]} / I_{A_{1g}} > 2$ at the 532-nm wavelength resonant excitation condition, with $I_{[2LA(M) + E_{2g}^1]}$ being the sum of the intensities in Raman modes 2LA(M) and E_{2g}¹ and $I_{A_{1g}}$ being the intensity of Raman mode A_{1g}⁷.

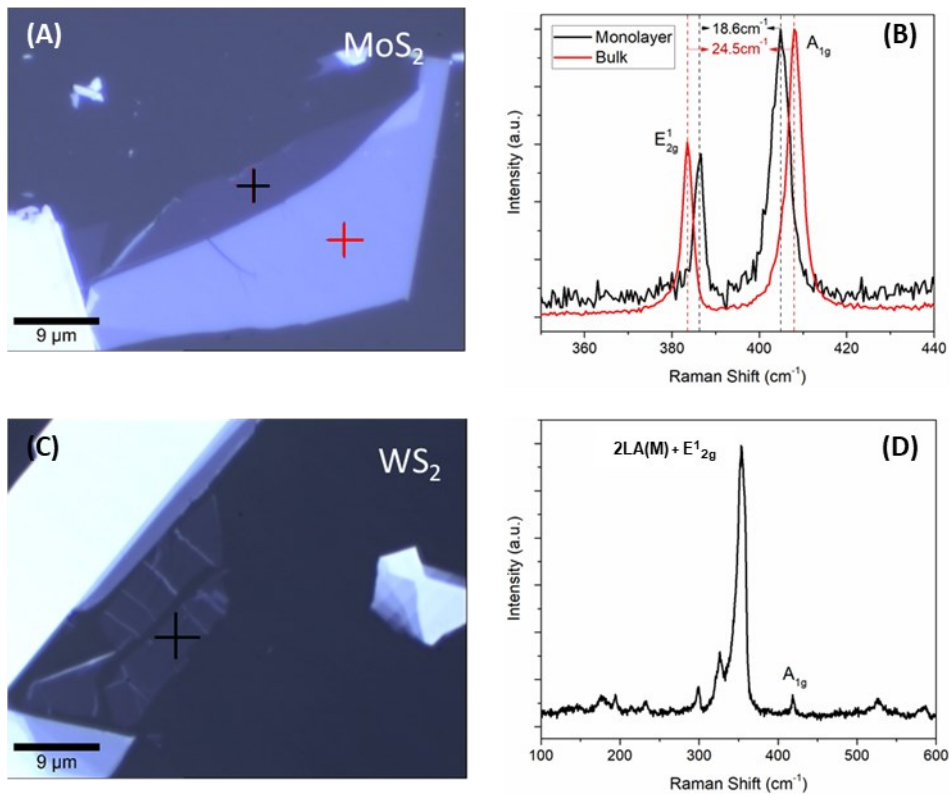


Figure S5: MoS₂ and WS₂ on glass optical characterization. Optical microscope images of MoS₂ (A) and WS₂ (C) deposited on glass. (B) & (D) Raman spectra obtained at the same color positions marked by a cross in (A) and (C), respectively. Raman data obtained at 532 nm with

0.5 s, 10 accumulations and 3.5 mW laser power for MoS₂; and 2 s integration time, 10 accumulations and 1.15 mW laser power for WS₂.

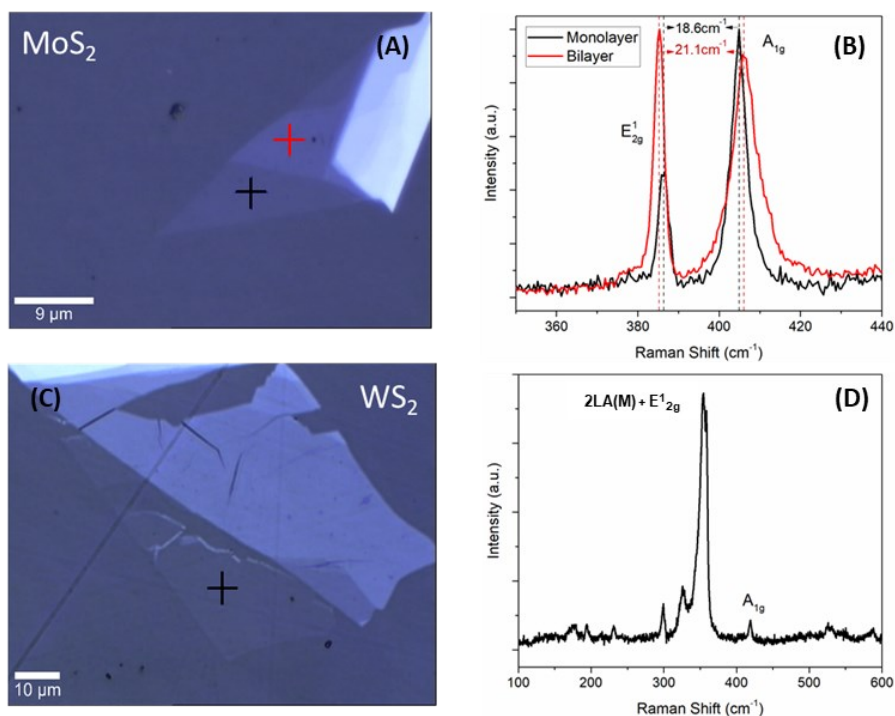


Figure S6: MoS₂ and WS₂ on FTO optical characterization. Optical microscope images of MoS₂ (A) and WS₂ (C) deposited on FTO. (B) & (D) Raman spectra obtained at the same color positions marked by a cross in (A) and (C), respectively. Raman data obtained at 532 nm with 2 s, 10 accumulations and 3.5mW laser power for MoS₂; and 2 s integration time, 10 accumulations and 1.15 mW laser power for WS₂.

To minimize possible substrate roughness variations, MoS₂ and WS₂ flakes were transferred to the same FTO substrate, shown in the optical microscope image of Figure S6. For the samples of TMDs on glass, the glass substrate was the same as the one used for FTO deposition.

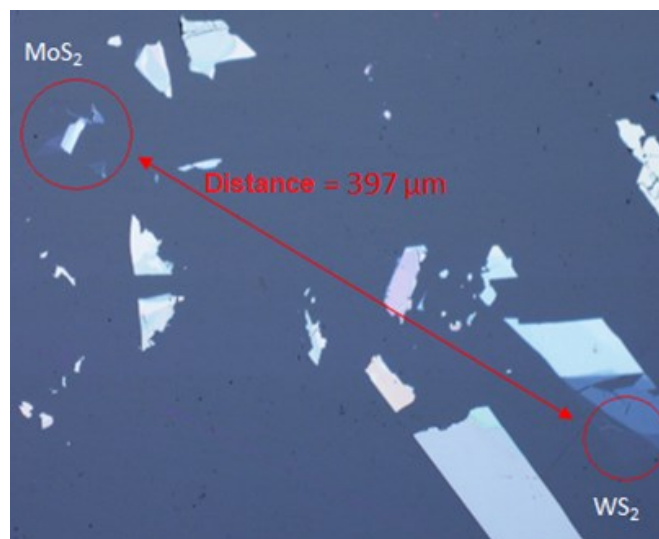


Figure S7: Optical microscope image of MoS₂ and WS₂ flakes deposited on the same FTO substrate. The red circle highlights the monolayer regions.

5. Sample imaging and flake location

Reflected THG can be observed overlaid on the linear optical image, shown in Figure S8. A red LED source, a CCD camera and some optics were used to optically image, in reflection, both the TMDC flakes and the THG beam profile generated by the pump laser. A neutral density filter is used to control the red LED light intensity (more attenuation on Figure S8(A) and less attenuation on Figure S8(B)), which allows for a better visualization of the THG spot. Also, adjusting the CCD camera's RGB response improves visualization. THG arises from both FTO and the 2D material (with the spot getting brighter on flakes), which is not a problem, since it is simply used for visualization. The yellow triangle in Figure S8(A) delimits the monolayer flake, which can be more easily seen in Figure S8(B).

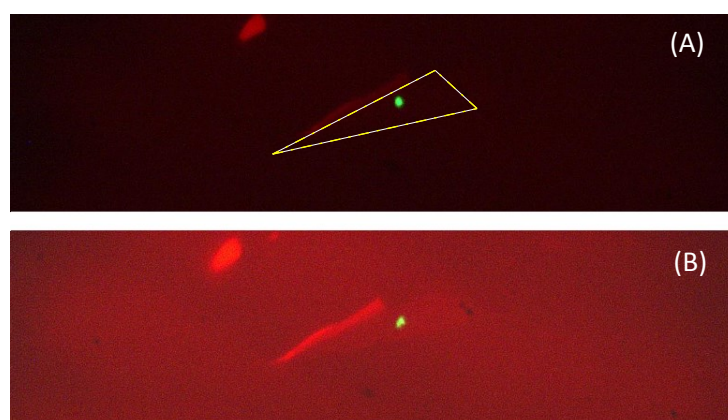


Figure S8. Optical image of the flakes under red LED light illumination and the THG beam. (A) Attenuated red LED light. The yellow triangle delimits the monolayer TMDC flake. (B) Higher LED light intensity on the sample.

6. SHG polarization dependence in FTO

As the FTO is deposited by sputtering, it tends to be amorphous, with the observed SHG component possibly arising from some local remnant (and variable) crystallinity^{8,9}. As a consequence, the SHG polarization dependence (parallel configuration) is variable (remaining inexistent in the perpendicular configuration), as shown in Figure S9, for multiple positions of the same substrate. For that reason, as mentioned in the manuscript, the analysis mainly focuses on the perpendicular polarization configuration, considered interference-free from the FTO SHG.

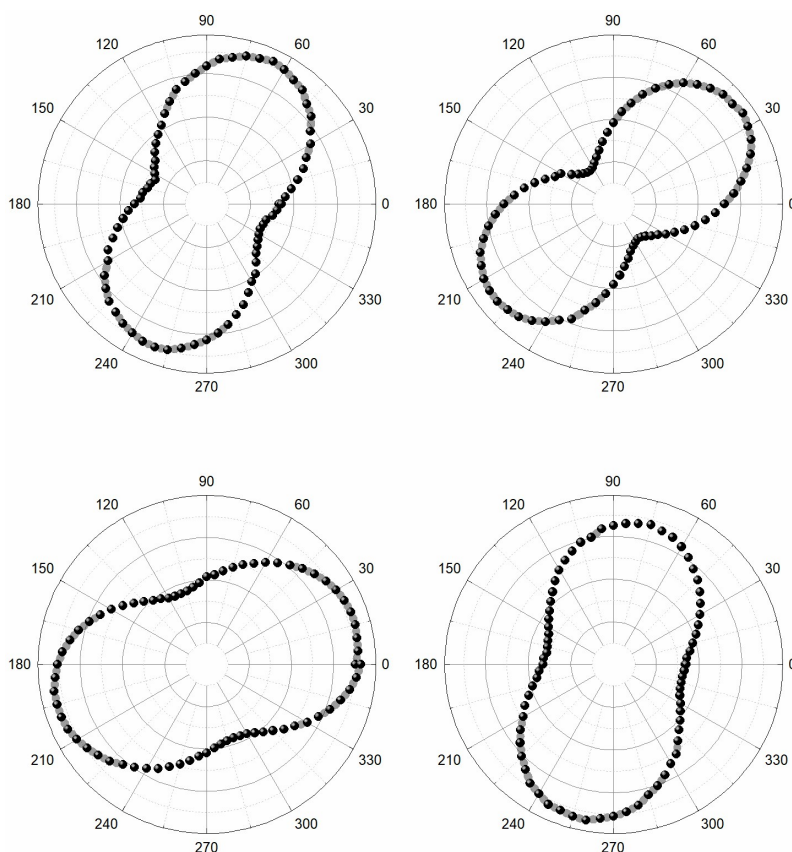


Figure S9. SHG intensity as a function of pump polarization angle in the parallel polarization configuration for FTO at different positions of the same substrate.

7. Theoretical curves for the SHG polarization dependence in the perpendicular configuration

For MoS₂ in the perpendicular configuration, the theoretical prediction is shown below, in Fig.S10. The red plot represents the SHG intensity as a function of the pump polarization angle for MoS₂/FTO and the black plot for MoS₂/Glass. Data has been shifted by 9° and 6° in the FTO and Glass plots, respectively, to reflect the experimental crystal orientations.

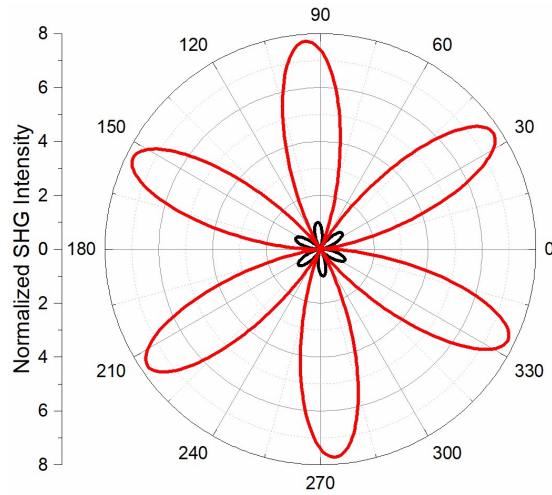


Figure S10. Theoretical prediction for MoS₂ on FTO (red) and Glass (black) in the perpendicular polarization.

For WS₂, theoretically predicting the SHG polarization dependence would only be meaningful in a strain-controlled experiment. Without the nature (uniaxial, biaxial), direction, and local strain amplitude, such calculation would be difficult and of limited applicability. For simplicity, we could assume the monolayer WS₂ is under uniaxial strain^{10,11}, however, a number of free-parameters would have to be implied, and no consistent model or useful data extracted, as more sophisticated methods would be necessary to model the nature of the strain in our samples.

8. SHG polarization dependence for TMDCs on Glass

MoS₂/Glass and WS₂/Glass in the parallel configuration present the same pattern and intensity as in the perpendicular configuration with a phase shift of 30°, as shown in the Fig. S11. The results for MoS₂/Glass can be observed in Fig. S11 (A) and WS₂/Glass in Fig. S11 (B).

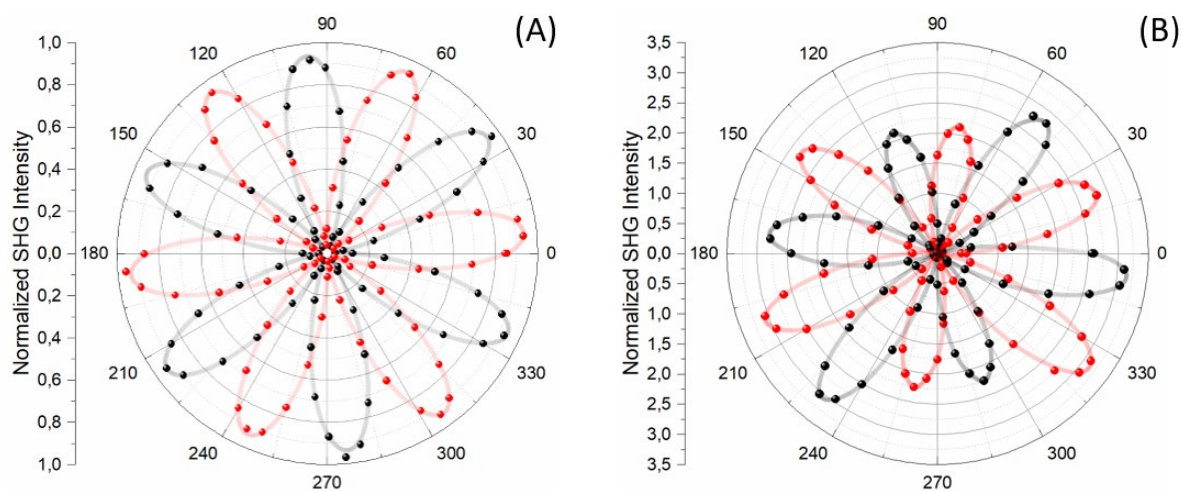


Figure S11. Polarized SHG as a function of pump polarization angle in the parallel polarization (red) and perpendicular polarization (black) configurations for MoS₂ (A) and WS₂ (B).

9. Photoluminescence measurements

During sample preparation, TMDC flakes were exfoliated on PDMS, which in contact with the desired substrates and then detached, transferred the monolayers to glass and FTO. The procedure relies on pressure applied during the transfer process, which can possibly deform the viscoelastic stamp, yielding stain¹². The origin of strain is usually attributed to the inherent lack of stiffness of PDMS. PDMS being soft can get slightly deformed during transfer by the pressure exerted upon contact with the target substrate, likely being the deformation source to induce strain in the flake being transferred^{12,13}.

In principle, and as already observed by others^{14–17}, the photoluminescence (PL) shift can be considered an indicator of how the electronic band structure is altered by the application of strain in TMDCs. In our case, PL for monolayer WS₂ was measured before and after the transfer process. Figure S12 shows the normalized PL for monolayer WS₂ on PDMS and after transferring to FTO (A) and Glass (B). It is possible to observe a shift in the PL peaks, both from 2.02 eV to 2.01 eV, compatible with tensile strain of less than 1% in monolayer WS₂¹⁴. This strain magnitude is compatible with the observed deformation in the SHG polarization dependent plots in Fig. 4(B)^{10,11}

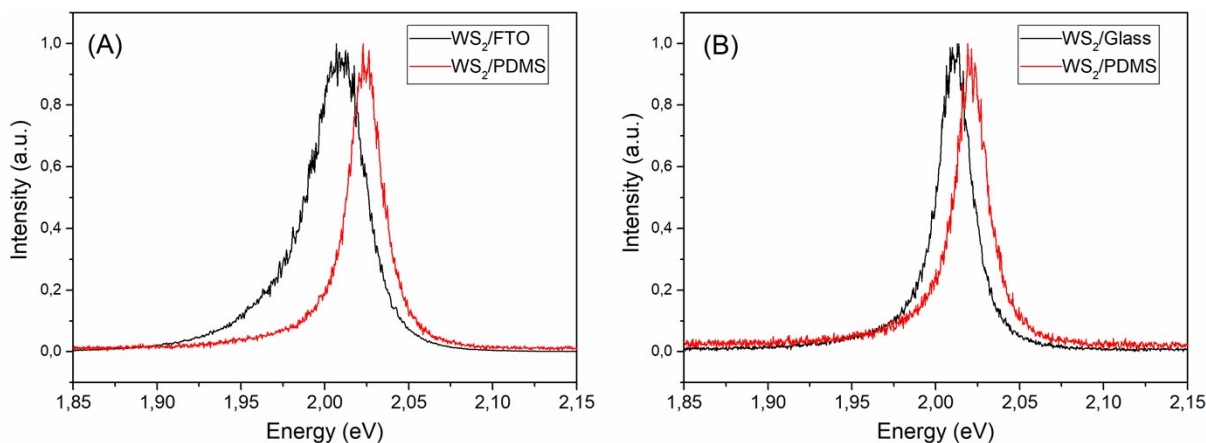


Figure S12. Normalized PL for WS₂ monolayers on PDMS (red curve) and after transferring to FTO (A) and Glass (B).

References:

- (1) Shen, Y. R. OPTICAL SECOND HARMONIC GENERATION AT INTERFACES. *Annu. Rev. Phys. Chem.* **1989**, *40*, 327–350.
- (2) Li, Y.; Heinz, T. F. Two-Dimensional Models for the Optical Response of Thin Films. *2D Mater.* **2018**, *5* (2).
- (3) Sipe, J. E. New Green-Function Formalism for Surface Optics. *J. Opt. Soc. Am. B* **1987**, *4* (4), 481.
- (4) Sipe, J. E.; Moss, D. J. Phenomenological Theory of Optical Second- and Third-Harmonic Generation from Cubic Centrosymmetric Crystals. *Phys. Rev. B* **1987**, *35* (3), 1129–1141.
- (5) Dean, J. J.; Van Driel, H. M. Graphene and Few-Layer Graphite Probed by Second-Harmonic Generation: Theory and Experiment. *Phys. Rev. B - Condens. Matter Mater. Phys.* **2010**, *82* (12), 1–10.
- (6) Lee, C.; Yan, H.; Brus, L. E.; Heinz, T. F.; Hone, J.; Ryu, S. Anomalous Lattice Vibrations of Single- and Few-Layer MoS₂. *ACS Nano* **2010**, *4* (5), 2695–2700.
- (7) Berkdemir, A.; Gutiérrez, H. R.; Botello-Méndez, A. R.; Perea-López, N.; Elías, A. L.; Chia, C. I.; Wang, B.; Crespi, V. H.; López-Urías, F.; Charlier, J. C.; et al. Identification of Individual and Few Layers of WS₂ Using Raman Spectroscopy. *Sci. Rep.* **2013**, *3*, 1–8.
- (8) Wang, Z.; Chen, C.; Wu, K.; Chong, H.; Ye, H. Transparent Conductive Oxides and Their Applications in Near Infrared Plasmonics. *Phys. Status Solidi Appl. Mater. Sci.* **2019**, *216* (5), 1–12.
- (9) Koirala, M. P.; Joshi, L. P. Structural and Optical Properties of Fluorine Doped Tin Oxide Thin Film Deposited by Home Built Spray Pyrolysis Unit. *Himal. Phys.* **2017**, *6*, 58–60.
- (10) Liang, J.; Zhang, J.; Li, Z.; Hong, H.; Wang, J.; Zhang, Z.; Zhou, X.; Qiao, R.; Xu, J.; Gao, P.; et al. Monitoring Local Strain Vector in Atomic-Layered MoSe₂ by Second-Harmonic Generation. *Nano Lett.* **2017**, *17* (12), 7539–7543.
- (11) Mennel, L.; Furchi, M. M.; Wachter, S.; Paur, M.; Polyushkin, D. K.; Mueller, T. Optical Imaging of Strain in Two-Dimensional Crystals. *Nat. Commun.* **2018**, *9* (516).
- (12) Castellanos-Gomez, A.; Buscema, M.; Molenaar, R.; Singh, V.; Janssen, L.; van der Zant, H. S. J.; Steele, G. A. Deterministic Transfer of Two-Dimensional Materials by All-Dry Viscoelastic Stamping. *2D Mater.* **2014**, *1*, 011002.
- (13) Jain, A.; Bharadwaj, P.; Heeg, S.; Parzefall, M.; Taniguchi, T.; Watanabe, K.; Novotny, L. Minimizing Residues and Strain in 2D Materials Transferred from PDMS.

- Nanotechnology* **2018**, *29*.
- (14) Pak, S.; Lee, J.; Lee, Y. W.; Jang, A. R.; Ahn, S.; Ma, K. Y.; Cho, Y.; Hong, J.; Lee, S.; Jeong, H. Y.; et al. Strain-Mediated Interlayer Coupling Effects on the Excitonic Behaviors in an Epitaxially Grown MoS₂/WS₂ van Der Waals Heterobilayer. *Nano Lett.* **2017**, *17* (9), 5634–5640.
 - (15) Aas, S.; Bulutay, C. Strain Dependence of Photoluminescence and Circular Dichroism in Transition Metal Dichalcogenides: A $k \cdot p$ Analysis. *Opt. Express* **2018**, *26* (22), 28672.
 - (16) Tyurnina, A. V.; Bandurin, D. A.; Khestanova, E.; Kravets, V. G.; Koperski, M.; Guinea, F.; Grigorenko, A. N.; Geim, A. K.; Grigorieva, I. V. Strained Bubbles in van Der Waals Heterostructures as Local Emitters of Photoluminescence with Adjustable Wavelength. *ACS Photonics* **2019**, *6*.
 - (17) Manzeli, S.; Allain, A.; Ghadimi, A.; Kis, A. Piezoresistivity and Strain-Induced Band Gap Tuning in Atomically Thin MoS₂. *Nano Lett.* **2015**, *15* (8), 5330–5335.